Title

Hippo pathway in cancer cells induces NCAM1+αSMA+ fibroblasts to modulate tumor microenvironment.

Journal

Communications Biology, 7(1)

Authors

Thinyakul, Chanida

Sakamoto, Yasuhisa

Shimoda, Mayuko

et al.

Publication Date

2024-10-17

DOI

10.1038/s42003-024-07041-4

Peer reviewed

communications biology

Article

https://doi.org/10.1038/s42003-024-07041-4

Hippo pathway in cancer cells induces NCAM1^{+}αSMA^{+} fibroblasts to modulate tumor microenvironment

Chanida Thinyakul[1,2], Yasuhisa Sakamoto[1,11], Mayuko Shimoda[1,11], Yanliang Liu[1], Suyanee Thongchot[2,3], Omnia Reda[4], Akihiro Nita[1,5], Romgase Sakamula[6], Somponnat Sampattavanich[6], Ayato Maeda[1], Paweenapon Chunthaboon[1], David Nduru[1], Mayumi Niimura[1], Yohei Kanamori[1], Peti Thuwajit[2], Keiichi I. Nakayama[7,8], Kun-Liang Guan[9], Yorifumi Satou[4], Chanitra Thuwajit[2] & Toshiro Moroishi[1,5,10] ✉

Cancer cells adeptly manipulate the tumor microenvironment (TME) to evade host antitumor immunity. However, the role of cancer cell-intrinsic signaling in shaping the immunosuppressive TME remains unclear. Here, we found that the Hippo pathway in cancer cells orchestrates the TME by influencing the composition of cancer-associated fibroblasts (CAFs). In a 4T1 mouse breast cancer model, Hippo pathway kinases, large tumor suppressor 1 and 2 (LATS1/2), promoted the formation of neural cell adhesion molecule 1 (NCAM1)$^{+}$alpha-smooth muscle actin (αSMA)$^{+}$ CAFs expressing the transforming growth factor-β, which is associated with T cell inactivation and dysfunction. Depletion of LATS1/2 in cancer cells resulted in a less immunosuppressive TME, indicated by the reduced proportions of NCAM1^{+}αSMA^{+} CAFs and dysfunctional T cells. Notably, similar Hippo pathway-induced NCAM1^{+}αSMA^{+} CAFs were observed in human breast cancer, highlighting the potential of TME-manipulating strategies to reduce immunosuppression in cancer immunotherapy.

Evasion of immune destruction is a hallmark of cancer, which enables the cancer cells to grow, disseminate within the body, and resist the effects of immunotherapy[1]. Therefore, strategies targeting the drivers of immune evasion may improve the efficacy of cancer immunotherapy. The tumor microenvironment (TME) is a complex ecosystem that plays a significant role in tumor progression and influences the effectiveness of therapeutic interventions. TME is composed of cancer cells and their environments with various cell types, including immune cells, endothelial cells, pericytes, and cancer-associated fibroblasts (CAFs). These components interact with each other and cancer cells, leading to the release of soluble factors that contribute to immune evasion[1,2].

CAFs, one of the most abundant stromal cells in the TME, play key roles in regulating the immune activity and response to immunotherapy[3,4]. CAFs differ from normal fibroblasts due to their increased extracellular matrix production and upregulated secretion of pro-tumor factors[3,5]. CAFs are suggested to create an immunosuppressive environment that contributes to a poor response to immunotherapy. However, growing evidence has shown the heterogeneity of CAFs in the TME. Some CAF subsets have tumor-promoting functions, whereas others CAF subsets exhibit tumor-suppressing functions. The abundance of CAFs or certain CAF subsets is associated with resistance to immunotherapy[5,6]. However, the underlying mechanisms by which cancer cell-intrinsic signaling orchestrates CAF to modulate immune activity remain largely unknown.

The Hippo pathway is an evolutionarily conserved signaling pathway that plays important roles in organ development, tissue homeostasis, regeneration, and cancer development[7,8]. The core of the mammalian Hippo pathway is the kinase cascade. In this cascade, mammalian STE20-like protein kinase 1 and 2 phosphorylate and activate large tumor suppressor 1 and 2 (LATS1/2). LATS1/2 kinases then phosphorylate two transcription cofactors, yes-associated protein (YAP) and transcriptional co-activator with PDZ-binding motif (TAZ, also known as WWTR1), inhibiting their activity. When YAP/TAZ are dephosphorylated, they move into the nucleus where they interact with the TEA domain transcription factor 1–4 to induce the expression of genes promoting cell proliferation[9,10]. Activation of LATS1/2 kinases (and inactivation of YAP/TAZ) represents the major functional output of the Hippo pathway. The Hippo pathway is suggested to play a tumor suppressor role[8]; however, growing evidence suggests that the role of the Hippo pathway in cancer is context-dependent[11,12]. Previously, we demonstrated that the inactivation of LATS1/2 enhances antitumor immunity and suppresses tumor growth, highlighting its implication for immunotherapy[13]. Deletion of LATS1/2 in cancer cells triggers the initiation of antitumor immune responses and induction of tumor-specific CD8^{+}

A full list of affiliations appears at the end of the paper. ✉e-mail: moroishi@kumamoto-u.ac.jp

T cells in lymphoid organs. However, whether alterations in the Hippo pathway in cancer cells influence the TME, especially the composition of CAFs, and how these changes impact the immune responses remain unknown.

In this study, we investigated whether the Hippo pathway in cancer cells regulates CAFs to modulate the immune activity in the TME using a syngeneic breast cancer model. Our findings revealed that deletion of LATS1/2 in 4T1 breast cancer cells shifted the CAF composition towards less immunosuppressive phenotypes, thereby alleviating the inhibition on $CD8^+$ T cells in the TME and facilitating tumor destruction. These results provide insights into the mechanism by which the Hippo signaling pathway in cancer cells regulates immune cell functions via communication with CAFs in the TME. Our findings also highlight a CAF composition pattern associated with immunostimulatory conditions, showing potential implications for the development of advanced cancer immunotherapies.

Results

Single-cell RNA sequencing (scRNA-seq) analysis reveals distinct compositions of CAFs between wild-type (WT) and LATS1/2-deficient breast cancer

To uncover the potential link between the Hippo pathway in cancer cells and CAFs in the TME, we first investigated whether deletion of the Hippo pathway kinases LATS1/2 in cancer cells alters the CAF compositions in the TME. We used a murine syngeneic breast cancer model (BALB/c mice with 4T1 breast cancer) with abundant stromal cells[14]. We generated LATS1/2 double-knockout (dKO) 4T1 breast cancer cells using clustered regularly interspaced short palindromic repeat (CRISPR)/CRISPR-associated protein 9 (Cas9) genome-editing approach[13]. Deletion of LATS1/2 was confirmed by its DNA mutation (Supplementary Fig. 1A) as well as the absence of protein expression and activity (Supplementary Fig. 1B). We observed that YAP phosphorylation levels were increased in response to LATS1/2-activating signals[15] in wild-type (WT) 4T1 cells, whereas LATS1/2-deletion abolished YAP phosphorylation as evident by phos-tag electrophoresis analysis. In 4T1 WT cells, YAP/TAZ were localized to the cytoplasm in response to filamentous actin disruption by latrunculin B (LatB; activates LATS1/2), whereas YAP/TAZ remained in the nucleus in LATS1/2 dKO cells under the same conditions (Supplementary Fig. 1C). Next, we transplanted equal numbers of WT or LATS1/2 dKO 4T1 breast cancer cells into the mammary fat pads of syngeneic BALB/c mice. Tumors were collected on day 16 post-transplantation. We confirmed that YAP/TAZ nuclear localization was also evident in LATS1/2 dKO 4T1 tumors in vivo (Supplementary Fig. 1D). Consistent with our previous observation[13], LATS1/2 deficiency reduced 4T1 breast tumor growth at this stage of tumor progression (Fig. 1A). To investigate CAF subpopulations in the TME, we conducted scRNA-seq analysis (Fig. 1B). To this end, either WT or LATS1/2 dKO 4T1 breast tumors were collected at 16 days after transplantation. Tumors were pooled from nine tumor-bearing mice for each condition and dissociated using an enzymatic reaction to obtain a single-cell tumor suspension. To enrich all possible stromal cells, tumor-dissociated cells were stained with markers for immune cells (CD45), epithelial cancer cells (epithelial cell adhesion molecule [EpCAM]), and endothelial cells (CD31), followed by cell sorting for $CD45^-EpCAM^-CD31^-$ stromal cells using flow cytometry (Fig. 1B and Supplementary Fig. 1E). We found that αSMA^+ stromal cells were increased in WT tumors compared with LATS1/2 dKO tumors, while $PDGFR^+$ stromal cells were reduced (Supplementary Fig. 1F). This tendency holds true even after cell sorting, suggesting that the cell sorting procedure had a minimal impact on the characteristics of each stromal cell population. Stromal cell-enriched samples were processed using 10X Chromium with a microfluidic platform and sequenced to profile single-cell transcriptomes. The matrix data from all replicate samples were integrated. After dimensionality reduction and clustering using principal component analysis (PCA), we visualized our stromal cluster using a uniform manifold approximation and projection (UMAP), which was broadly unified into four groups based on the expression of cell type-specific markers: immune cells (protein tyrosine phosphatase receptor type C [*Ptprc*]), pericytes (regulator of G protein signaling 5 [*Rgs5*]), cancer cells with loss of EpCAM expression (keratin 7 [*Krt7*] and *Krt8*), and fibroblasts (podoplanin [*Pdpn*] and platelet-derived growth factor receptor alpha [*Pdgfra*]) (Fig. 1C and Supplementary Fig. 2). Since we observed a certain amount of contamination of cancer cells in the stromal cluster, we re-clustered the $Pdpn^+$ population to further characterize the CAFs, dividing them into six different clusters (Fig. 1D). A heat map of the top 10 markers in each CAF cluster demonstrated that each CAF subset had a distinct transcriptional expression pattern (Fig. 1E). Gene ontology (GO) analysis indicated that each CAF subpopulation exhibited distinct characteristics, supporting CAF heterogeneity (Fig. 1F and Supplementary Data 1). Cluster 0 CAFs expressed *Pi16*, *Ly6c1*, and stemness genes (*Cd34* and *Ly6a*), suggesting that their characteristics were close to those of the reported steady-state fibroblast cluster[16] (Fig. 1G). In contrast, cluster 1 CAFs expressed markers of myofibroblasts: *Spp1*, *Tagln*, and *Acta2* encoding for α-smooth muscle actin (αSMA) and a well-characterized pro-fibrotic factor, *Ccn2*, encoding for the connective tissue growth factor (CTGF)[17]. Cluster 2 CAFs showed high expression of *Cxcl14*, a cytokine that promotes monocyte migration and acts in an autocrine manner to promote fibroblast proliferation and migration[18]. Additionally, cluster 2 CAFs uniquely enriched for the GO term "histone binding" (Fig. 1F), the molecular function connected to the induction of myofibroblast differentiation[19,20], suggesting that cluster 2 CAFs might undergo an intermediate state during fibroblast conversion. Cluster 3 CAFs exhibit high expression of myeloid chemoattractant genes (*Saa3* and *Ccl2*)[21–23]. Cluster 4 CAFs showed high expression of the RNA-binding protein *Hnrnpa1*. Unlike other clusters, cluster 4 CAFs were not enriched for "extracellular matrix structural constituent" (Fig. 1F), suggesting that cluster 4 CAFs were not the main contributor to ECM (extracellular matrix) structure. Cluster 5 CAFs predominantly expressed cytokine *Cxcl12*, which is expressed in the iCAF subset and involved in myeloid cell recruitment[24]. Taken together, our data suggest the presence of distinct subsets of CAFs in WT and LATS1/2 dKO breast tumors.

LATS1/2 in cancer cells increases the proportion of $NCAM1^+\alpha SMA^+$ CAF subpopulation

To evaluate the changes in CAF composition induced by LATS1/2 deletion in cancer cells, we compared the abundance of CAF clusters derived from WT and LATS1/2 dKO 4T1 breast tumors. We found that LATS1/2 WT and dKO tumors exhibited different proportions of CAF subsets (Fig. 2A). The proportions of CAF clusters 1 and 2 were reduced by 77% and 55%, respectively, in LATS1/2 dKO tumors compared to WT tumors. In contrast, there was a 1.4 times and 3.5 times increase in the number of clusters 0 and 5, respectively, in LATS1/2 dKO tumors (Fig. 2B). These results suggest that cancer cell-intrinsic LATS1/2 induces CAFs to be categorized into clusters 1 and 2, while reducing cluster 5 CAFs. Since clusters 1 and 2 demonstrated marked differences between the WT and LATS1/2 dKO TME, we focused on those clusters for further study. The scRNA-seq data revealed that *Ncam1* and *Acta2* were predominantly expressed in clusters 1 and 2 CAFs, implying their application as markers for clusters 1 and 2 (Fig. 2C). αSMA (encoded by *Acta2*) is a well-known marker of myofibroblasts[25,26]. NCAM1 (neural adhesion molecule-1) is a cell adhesion protein expressed in a subset of CAFs implicated in the immune response in pancreatic ductal adenocarcinoma[27]. We reanalyzed the scRNA-seq datasets obtained from mouse MMTV-PyMT breast tumors[28] and found that *Ncam1* was specifically expressed in mechanoresponsive (MR) CAFs that share similar characteristics with myofibroblasts (Supplementary Fig. 3A). These results indicate that *Ncam1* is commonly expressed in the CAF subset with a myofibroblast phenotype in different mouse breast tumor models. Indeed, CAFs coexpressing *Ncam1* and *Acta2* were enriched in Clusters 1 and 2 (Fig. 2D and Supplementary Fig. 3B). The proportion of the $NCAM1^+\alpha SMA^+$ CAFs identified through scRNA-seq analysis was validated using flow

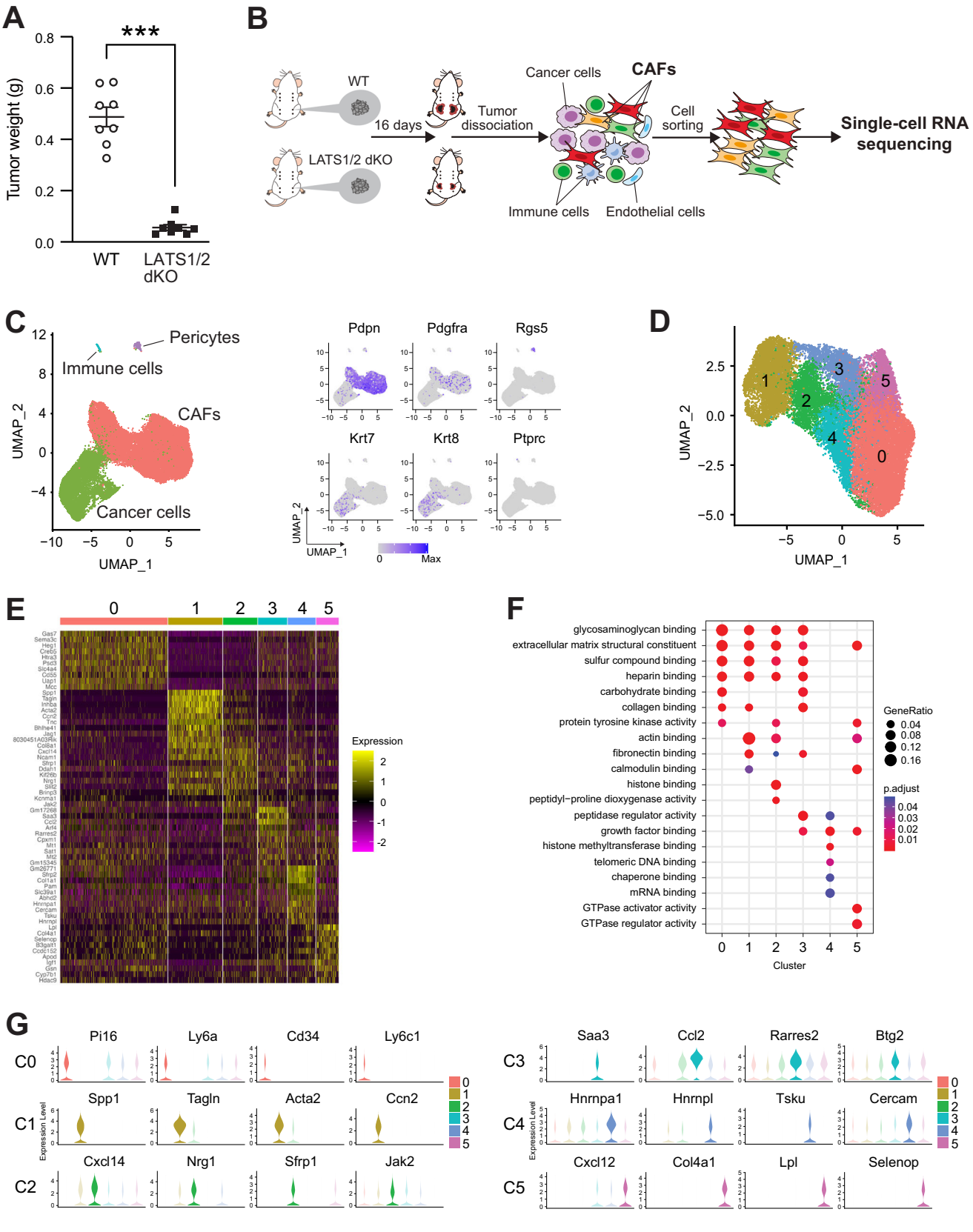

cytometry and immunohistochemistry analysis. As *Pdpn* was expressed in all CAF subsets (Supplementary Fig. 3C), we used PDPN as a marker for CAF enrichment. Consistent with scRNA-seq data, flow cytometry analysis revealed that the proportion of NCAM1$^+$αSMA$^+$ CAFs was reduced in LATS1/2 dKO tumor tissues (Fig. 2E). Immunofluorescence analysis revealed that NCAM1$^+$αSMA$^+$ cells showed spindle-like fibroblast morphology (Fig. 2F). Together, our data suggest that LATS1/2 in cancer cells induces NCAM1$^+$αSMA$^+$ CAF formation in the TME.

Fig. 1 | Distinct subpopulations of cancer-associated fibroblasts (CAFs) between wild-type (WT) and large tumor suppressor 1 and 2 (LATS1/2)-deficient breast cancer cells revealed via single-cell RNA sequencing (scRNA-seq) analysis. **A** BALB/c mice were injected with WT or LATS1/2 double-knockout (dKO) 4T1 breast cancer cells, and tumor weight was determined 16 days after transplantation. Data are represented as the mean ± standard error of the mean (SEM); $n = 8$ tumors for each WT or LATS1/2 dKO. ***$p < 0.001$, Mann–Whitney test. **B** Schematic illustration of the workflow of scRNA-seq analysis of CAFs derived from WT or LATS1/2 dKO 4T1 breast tumors. **C** Uniform manifold approximation and projection (UMAP) plot showing all cells from both WT and LATS1/2 dKO samples. **D** UMAP plot showing six distinct CAF clusters. **E** Heatmap showing differential expression of the top 10 markers in each mouse breast CAF cluster. **F** Gene Ontology (GO) analysis plots showing the top 20 GO terms (molecular function) among mouse breast CAF clusters. **G** Violin plots showing the differential marker expression in each mouse breast CAF cluster. Colors correspond to the indicated CAF cluster in the UMAP plot of CAFs shown in **D**.

NCAM1$^+$αSMA$^+$ CAFs exhibit myofibroblast phenotypes and express T cell regulation-related genes

We next characterized the NCAM1$^+$αSMA$^+$ CAFs by comparing their transcriptome with their non-NCAM1$^+$αSMA$^+$ counterpart using scRNA-seq data. The heatmap of the top 20 markers of each CAF subset suggested that NCAM1$^+$αSMA$^+$ CAFs and their counterpart showed distinct transcriptional expression pattern (Fig. 3A and Supplementary Table 1). To delve into the characteristics of NCAM1$^+$αSMA$^+$ CAFs in more detail, we took advantage of previously published scRNA-seq datasets on well-studied CAF subsets in pancreatic ductal adenocarcinoma; myofibroblastic CAFs (myCAFs)[29], inflammatory CAFs (iCAFs)[29], antigen-presenting CAFs (apCAFs)[29], and leucine-rich repeat containing 15 (LRRC15)$^+$ CAFs[30]. MyCAFs exhibit myofibroblast phenotypes, producing and remodeling ECM[29,31]. iCAFs secrete high levels of inflammatory cytokines and chemokines[29,31]. ApCAFs can present antigens to T cells and induce regulatory T cell differentiation[29,32]. LRRC15$^+$ CAFs are myofibroblast-like CAFs that suppress CD8$^+$ T cell function in pancreatic ductal adenocarcinoma[30]. We performed gene set enrichment analysis (GSEA) to compare transcriptional expression patterns of NCAM1$^+$αSMA$^+$ CAFs to those of previously characterized CAF subsets. To this end, we reanalyzed the scRNA-seq dataset of Elyada et al. [29]. to extract the gene signatures of myCAFs, iCAFs, and apCAFs (Supplementary Fig. 4A, B). For the gene signature of LRRC15$^+$ CAFs, we used the marker gene list provided by Krishnamurty et al. [30]. GSEA revealed that NCAM1$^+$αSMA$^+$ CAFs show positive enrichment scores for both the myCAF and LRRC15$^+$ CAF signature gene sets, but not for iCAF nor apCAF, suggesting that NCAM1$^+$αSMA$^+$ CAFs exhibit a transcriptional similarity to myCAFs and LRRC15$^+$ CAFs, both of which possess myofibroblast-like phenotypes (Fig. 3B). Indeed, GO analysis revealed that NCAM1$^+$αSMA$^+$ CAFs exhibited enrichment in terms, such as "regulation of response to wounding," "regulation of wound healing," "cell-substrate adhesion," and "regulation of cell-substrate adhesion," indicating myofibroblast features (Fig. 3C and Supplementary Data 2). Additionally, NCAM1$^+$αSMA$^+$ CAFs shared common genes with mouse breast cancer MR CAFs (*Spp1*, *Thbs2*, *Cdh11*, and *Lrrc15*), which exhibit a myofibroblast phenotype[28] (Supplementary Fig. 4C). NCAM1$^+$αSMA$^+$ CAFs exhibited upregulation of myofibroblast-related genes compared to non-NCAM1$^+$αSMA$^+$ fibroblasts, further confirming the presence of myofibroblast features (Fig. 3D). Therefore, NCAM1$^+$αSMA$^+$ CAFs exhibit myofibroblast characteristic and may regulate T cell function, as shown in LRRC15$^+$ CAFs[30]. Interestingly, we also found that NCAM1$^+$αSMA$^+$ CAFs expressed high levels of T cell regulation-related genes compared to non-NCAM1$^+$αSMA$^+$ CAFs (Fig. 3E). Together, these data suggest that NCAM1$^+$αSMA$^+$ CAFs exhibit myofibroblast characteristics and may regulate T cells.

NCAM1$^+$αSMA$^+$ CAFs express transforming growth factor β (TGFβ)

As NCAM1$^+$αSMA$^+$ CAFs express T cell regulation-related genes and exhibit a transcriptional similarity to LRRC15$^+$ CAFs, which inhibit CD8$^+$ T cell function[30], we hypothesized that NCAM1$^+$αSMA$^+$ CAFs suppress T cell function in the TME of the breast tumor model. Notably, we found that *Tgfb1* and *Tgfb2*, cytokines known to inhibit the function of effector T cells[33], were specifically expressed in NCAM1$^+$αSMA$^+$ CAFs, but not non-NCAM1$^+$αSMA$^+$ fibroblasts (Fig. 4A). In addition, NCAM1$^+$αSMA$^+$ CAFs expressed *Thbs1* (encoding for thrombospondin-1) and *Mmp14*, which play key roles in the activation of TGFβ[34,35]. Immunofluorescence analysis using serial tissue sections with co-staining for NCAM1/αSMA and αSMA/TGFβ1 confirmed TGFβ1 expression in NCAM1$^+$αSMA$^+$ fibroblasts in tumor tissues (Fig. 4B and Supplementary Fig. 5), with approximately 20–50% of αSMA$^+$ populations express detectable levels of TGFβ1 (Fig. 4C). We further investigated whether TGFβ-expressing fibroblasts suppress CD8$^+$ T cell function by conducting in vitro coculture experiments (Fig. 4D). To test this, we generated biologically active TGFβ1-overexpressing fibroblasts via site-directed mutagenesis to convert cysteines at amino acid positions 223 and 225 to serines, which resulted in the constitutive release and secretion of the biologically active TGFβ1[36]. TGFβ1-overexpressing fibroblasts expressed high levels of pro-TGFβ1 (a large N-terminal portion of the precursor) and mature-TGFβ1 (containing the bioactive portion required for the receptor binding) (Fig. 4E, left). We further detected mature-TGFβ1 in the supernatant collected from TGFβ1-overexpressing fibroblast cells, suggesting that TGFβ1-overexpressing fibroblasts express and secrete mature TGFβ1 proteins (Fig. 4E, right). To examine whether TGFβ1-overexpressing fibroblasts suppress CD8$^+$ T cell function, we activated splenic T cells using CD3/CD28 beads and co-cultured them with TGFβ1-overexpressing fibroblasts (Fig. 4D). After three days, T cells were re-stimulated with a combination of phorbol 12-myristate 13-acetate (PMA) and ionomycin, and their interferon γ (IFNγ) and granzyme B protein expression levels were determined via flow cytometry. Upon co-culturing with TGFβ1-overexpressing fibroblasts, CD8$^+$ T cells showed a significant reduction in IFNγ and granzyme B expression levels compared to the levels observed in the cells co-cultured with control fibroblasts, indicating that TGFβ-expressing fibroblasts inhibit CD8$^+$ T cell function (Fig. 4F). Together, these data imply that NCAM1$^+$αSMA$^+$ CAFs express TGFβ, which has the potential to suppress effector T cells.

Dysfunctional CD8$^+$ T cells are abundant in NCAM1$^+$αSMA$^+$ CAFs-enriched tumors

Next, we investigated whether CD8$^+$ T cells in the NCAM1$^+$αSMA$^+$ CAFs-enriched tumors are dysfunctional. CAFs with αSMA expression were observed in the proximity of CD8$^+$ T cells, suggesting potential interactions between them (Fig. 5A). We found a significant increase in the population of CD8$^+$ T cells expressing the effector cytokine, interferon-gamma (IFNγ), in LATS1/2 dKO tumors compared to WT tumors (Fig. 5B). In contrast, PD1$^+$CD8$^+$ T cells with high expression of TIM3, a surface receptor associated with T-cell dysfunction[37], were more abundant in WT tumors than in LATS1/2 dKO tumors (Fig. 5C). These observations suggest that LATS1/2 in cancer cells induces T cell dysfunctionality.

NCAM1$^+$αSMA$^+$ CAFs are observed in human breast cancer

To test the presence of NCAM1$^+$αSMA$^+$ CAFs in human breast cancer, we performed immunofluorescence staining of NCAM1 and αSMA using a small cohort of patients with breast cancer. We observed the co-expression of NCAM1 (with a membrane staining pattern) and αSMA (showing cytoplasmic staining) with fibroblast morphology in three out of the 27 breast cancer samples (Fig. 6A, Supplementary Fig. 6, and Supplementary Table 2). Additionally, we reanalyzed the data from a previously published study on scRNA-seq in human patients with breast cancer by Wu and colleagues[38] (Supplementary Fig. 7). We performed cell-type label transfer and projected our mouse breast CAF scRNA-seq clusters onto the UMAP

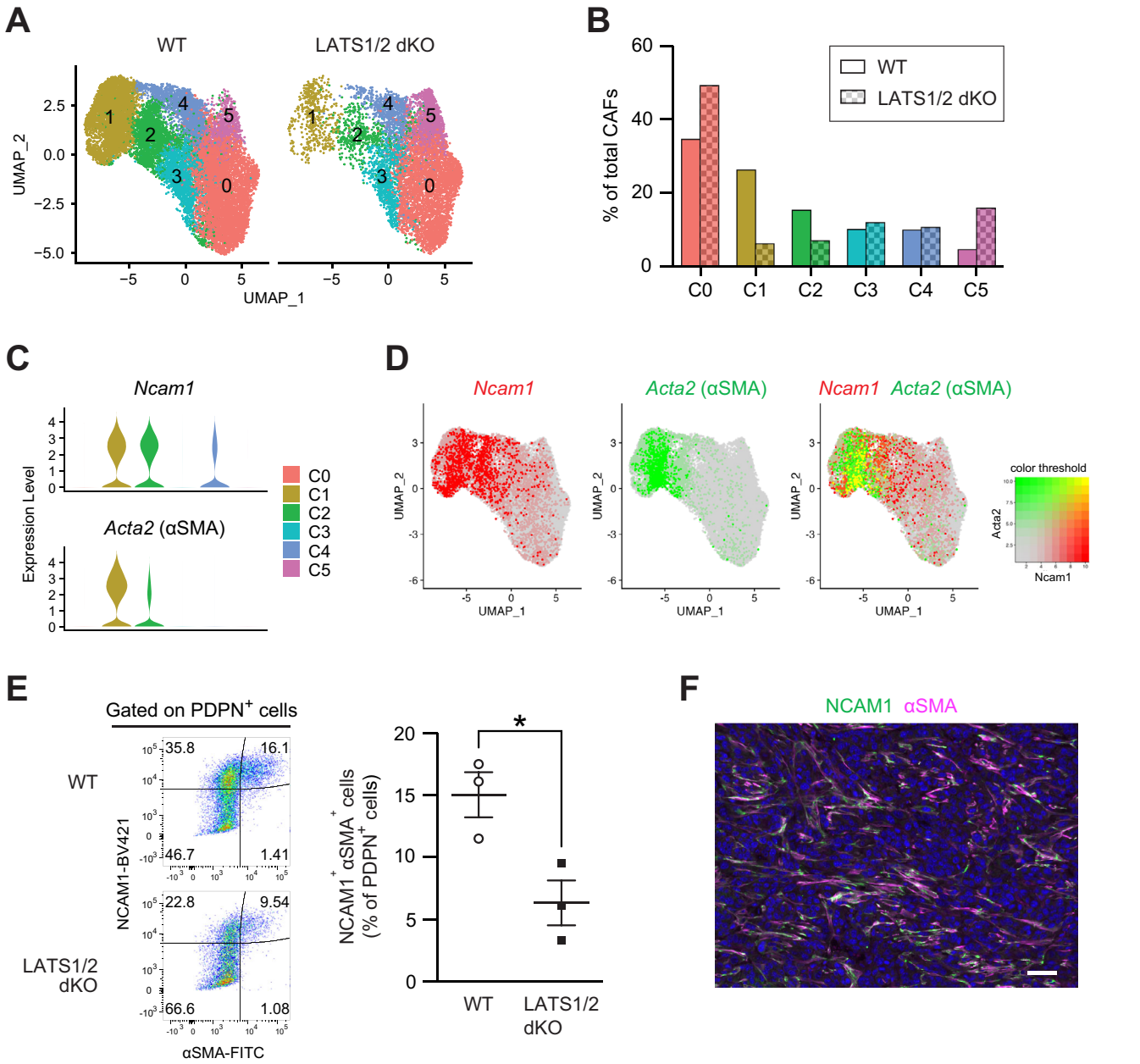

Fig. 2 | LATS1/2 in cancer cells increases the proportion of neural cell adhesion molecule 1 (NCAM1)$^+$alpha-smooth muscle actin (αSMA)$^+$ CAF subpopulation. **A** UMAP plot showing the CAF clusters from WT or LATS1/2 dKO 4T1 breast tumors. **B** Bar plot showing the percentage of each CAF cluster among total CAFs from WT or LATS1/2 dKO tumors shown in **A**. **C** Violin plots showing the differential expression of *Ncam1* or *Acta2* in each mouse breast CAF cluster. Colors correspond to the indicated CAF cluster in the UMAP plot of CAFs shown in **A**. **D** Feature plot showing single cells with *Ncam1* and *Acta2* co-expression on the UMAP plot of mouse breast CAF clusters. Color threshold corresponds to the expression level of the indicated gene. **E** WT or LATS1/2 dKO 4T1 breast cancer cells were injected into BALB/c mice, and tumors were subjected to flow cytometry analysis 16 days after transplantation. Representative flow cytometry plots showing the frequency of NCAM1$^+$αSMA$^+$ CAFs are shown in the left panel. Cells were gated on CD45$^-$epithelial cell adhesion molecule (EpCAM) $^-$CD31$^-$podoplanin (PDPN)$^+$ cells. Data are represented as the mean ± SEM of the percentage of NCAM1$^+$αSMA$^+$ CAFs in tumors among total CD45$^-$EpCAM$^-$CD31$^-$PDPN$^+$ cells; $n = 3$ samples; pooled 4–11 tumors in each group. *$p < 0.05$, unpaired two-tailed *t*-test. **F** Representative immunofluorescence image of mouse breast tumor tissues. Paraffin-embedded sections of WT 4T1 breast tumors were subjected to immunostaining analysis of NCAM1 (green) and αSMA (magenta) or 4',6-diamidino-2-phenylindole (DAPI) for DNA (blue). Data are representative of three tumors. Scale bar = 50 μm.

structure of human CAF clusters based on the similarity of gene expression patterns using Seurat's reference mapping approach[39]. We found that our mouse NCAM1$^+$αSMA$^+$ CAFs showed transcriptomic similarity to the UMAP positions of human breast CAF clusters 1, 4, and 7 (Fig. 6B). Notably, these human CAF clusters expressed myofibroblast gene signatures (Fig. 6C) and were identified as myofibroblast-like CAFs[38]. Altogether, these data suggest high transcriptional similarity between mouse NCAM1$^+$αSMA$^+$ CAFs and myofibroblast-like CAFs in human breast cancer.

Discussion

Understanding how cancer cell-intrinsic signaling orchestrates the TME to modulate immune activity could provide strategies to achieve immune destruction and resolve immunotherapy resistance. In this study, we

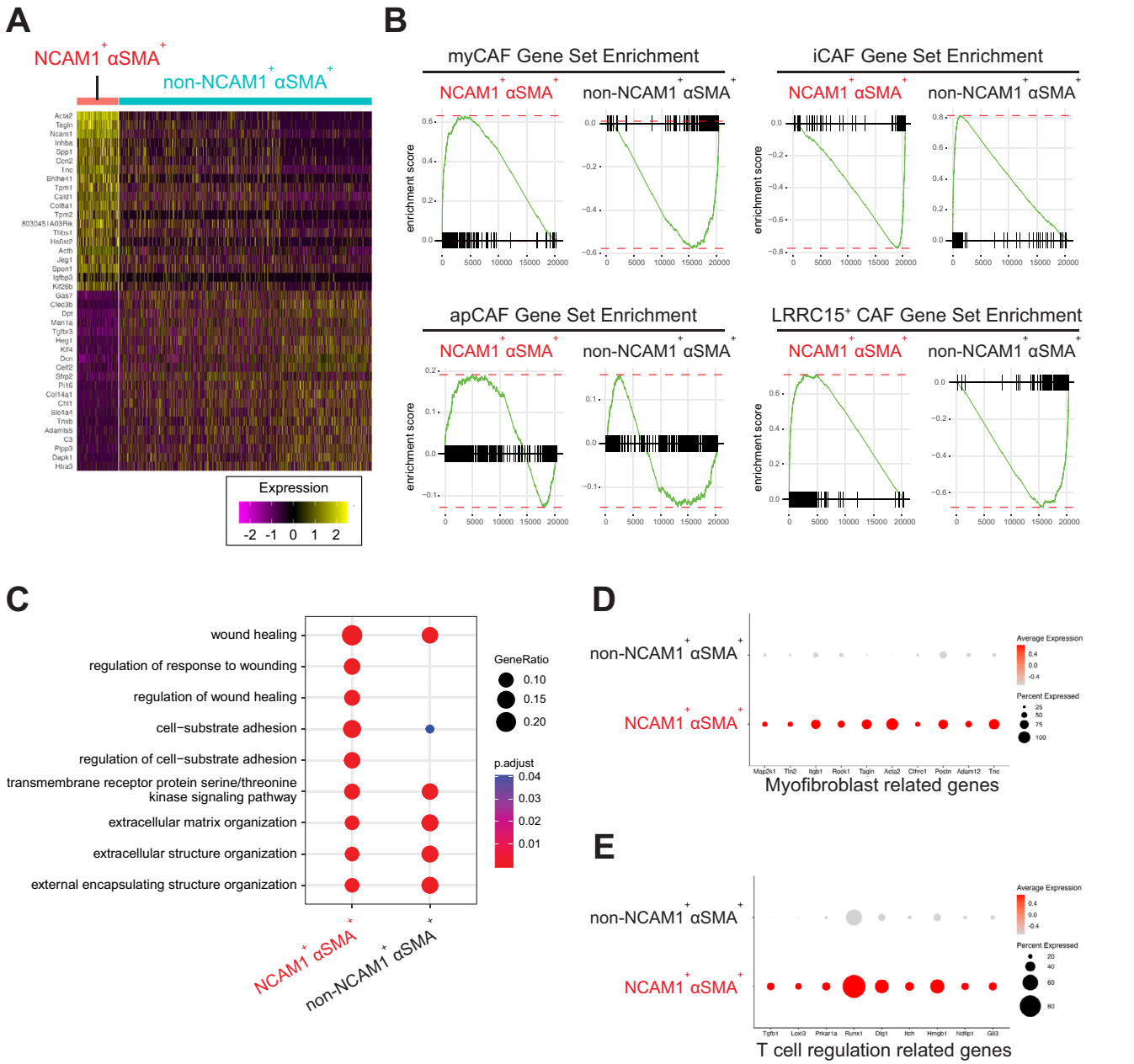

Fig. 3 | NCAM1$^+$αSMA$^+$ CAFs exhibit myofibroblast phenotypes and express T cell regulation-related genes. A Heatmap showing the differential expression of the top 20 markers of the mouse breast NCAM1$^+$αSMA$^+$ or non-NCAM1$^+$αSMA$^+$ CAF subpopulations. **B** Gene set enrichment analysis of the signature gene sets of myofibroblastic CAFs (myCAFs), inflammatory CAFs (iCAFs), antigen-presenting CAFs (apCAFs), or leucine-rich repeat containing 15 (LRRC15)$^+$ CAFs in NCAM1$^+$αSMA$^+$ or non-NCAM1$^+$αSMA$^+$ CAF subpopulations. **C** GO analysis plots showing the top nine GO terms (biological process) between NCAM1$^+$αSMA$^+$ and non-NCAM1$^+$αSMA$^+$ CAF subpopulations. Dot plot showing the differential average expression level of (**D**) myofibroblast related genes or (**E**) T cell regulation-related genes between NCAM1$^+$αSMA$^+$ and non-NCAM1$^+$αSMA$^+$ CAF subsets. Dot size corresponds to the percentage of cells expressing the gene in each CAF subset. Color indicates the average expression level.

demonstrate that 4T1 breast cancer cells' intrinsic LATS1/2 modulate the composition of CAFs and suppress T cell functions. LATS1/2 deletion in cancer cells results in the reduction of the NCAM1$^+$αSMA$^+$ CAF subpopulation and the enhancement of CD8$^+$ T cell function, leading to tumor suppression. These results suggested that the cancer-intrinsic Hippo pathway plays a significant role in immune evasion. We have previously shown that inactivation of LATS1/2 in cancer cells can stimulate antitumor immunity by enhancing antigen cross-presentation and promoting the clonal expansion of tumor-specific CD8$^+$ T cells[13]. These processes induce cytotoxic T lymphocytes (CTLs) in the lymphoid organs. Together, our data indicate that the immunosuppressive effects of LATS1/2 are controlled from the early stage of tumor formation and persist throughout tumor progression, explaining the mechanism underlying the long-term suppression of tumor growth by LATS1/2 deletion. Our study sheds light on the effect of LATS1/2 inactivation on cancer cells in the TME.

In this study, we identified six transcriptionally distinct subpopulations of CAFs in 4T1 mouse breast tumors. Three CAF subpopulations are modulated by cancer cell-intrinsic LATS1/2; the induction of cluster 1 and cluster 2 CAFs, specifically NCAM1$^+$αSMA$^+$ CAFs, and the reduction of cluster 5 CAFs. One may speculate that these three CAF subsets are also present in other mouse breast tumor models or other tumor types. Foster et al. identified three distinct CAF clusters in an MMTV-PyMT mouse breast tumor model: steady state-like (SSL), MR, and immunomodulatory (IM) CAFs[28]. In pancreatic ductal adenocarcinoma, a recent study suggested

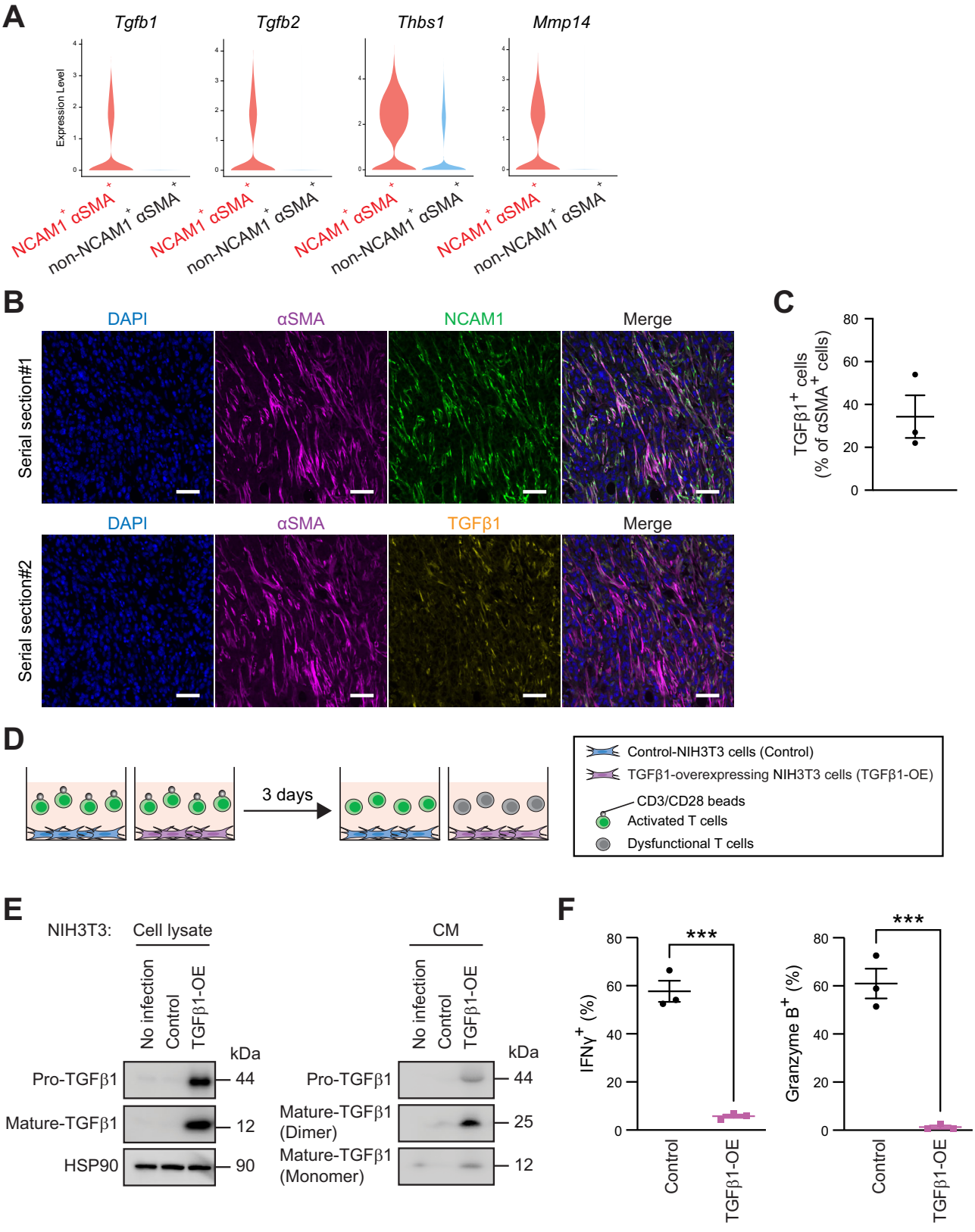

three distinct CAF subpopulations: myofibroblasts (myCAFs), inflammatory CAFs (iCAFs), and antigen-presenting CAFs (apCAFs)[29]. Accordingly, cluster 1 CAFs shared common myofibroblast characteristics with pancreatic myCAFs (Supplementary Fig. 8) and shared common genes (*Spp1, Thbs2, Cdh11, Lrrc15*) with the breast MR CAF cluster (Supplementary Fig. 4C). Cluster 2 CAFs also shared common myofibroblast characteristics with myCAFs (Supplementary Fig. 8) and shared common genes with MR CAFs, but to a lesser extent than cluster 1 CAFs (Supplementary Fig. 4C). We speculated that cluster 2 may be an intermediate state of myofibroblast cluster 1 CAFs. Further investigation is needed to clarify the characteristics

Fig. 4 | NCAM1$^+$αSMA$^+$ CAFs express TGFβ and induce dysfunctional CD8$^+$ T cells. A Violin plots showing the differential expression of the indicated gene in NCAM1$^+$αSMA$^+$ or non-NCAM1$^+$αSMA$^+$ CAF subpopulations. **B** Representative immunofluorescence images of mouse breast tumor samples. Two serial sections of paraffin-embedded tissues from WT 4T1 breast tumors were subjected to two sets of immunostaining. Serial section #1 (top panel): αSMA (magenta), NCAM1 (green), and DAPI (blue); serial section #2 (bottom panel): αSMA (magenta), TGFβ1 (yellow), and DAPI (blue). Data are representative of three tumors. Scale bar = 50 μm. **C** Quantitative analysis of data in **B** is represented as the mean ± SEM; $n = 3$ tumors. **D** Schematic illustration of the ex vivo co-culture of the activated T cells and TGFβ1-overexpressing fibroblasts. Splenocytes were seeded on top of the attached NIH3T3 fibroblasts with empty vector (control) or TGFβ1-overexpressing NIH3T3 cells (TGFβ1-OE). Splenic T cells were stimulated with CD3/CD28 beads. After 72 h, co-culturing with TGFβ1-OE fibroblasts was expected to suppress T cell function, which was determined via evaluation of T cell activation markers using flow cytometry. **E** Cell lysate (left) or culture medium (CM) (right) from NIH3T3 cells with no infection, infection with empty vector (control), or infection with TGFβ1-overexpressing vector (TGFβ1-OE) was subjected to immunoblot analysis with antibodies against TGFβ1 or HSP90. Immunoblot analysis of CM samples was performed under non-reducing conditions. **F** Splenocytes from C57BL/6 mice were co-cultured with the control or TGFβ1-overexpressing NIH3T3 fibroblasts in the presence of CD3/CD28 beads for 72 h as shown in **D**. Splenocytes were re-stimulated with a combination of phorbol 12-myristate 13-acetate (PMA) and ionomycin and subjected to flow cytometry analysis. Frequency of CD8$^+$ T cells expressing interferon γ (IFNγ) or granzyme B was then determined. Data are represented as the mean ± SEM of biological triplicates. ***$p < 0.001$, unpaired two-tailed t-test.

and biological functions of cluster 2 CAFs. Cluster 5 CAFs have similar transcriptional profiles to pancreatic iCAFs (Supplementary Fig. 8) and express *Cxcl12*, an immunoregulatory cytokine expressed by iCAF and breast IM CAFs[28,29]. Our data validated the conservation of CAF clusters regulated by cancer cell-intrinsic LATS1/2 (myofibroblast cluster 1 and 2 CAFs and immune regulation cluster 5 CAFs) across different breast tumor models and different cancer types. The variety of CAFs in the TME is influenced by the diversity of cancer cells. Therefore, certain subpopulations of cancer cells may secrete different sets of cytokines, growth factors, and other signaling molecules and remodel the ECM, promoting the transition of normal fibroblasts to different types of CAFs. In this context, we demonstrated that cancer cells with active LATS1/2 induced the immunosuppressive clusters 1 and 2 CAFs, whereas those with inactive LATS1/2 led to the formation of cluster 5 CAFs. Although it remains unclear how cancer cells with varying LATS1/2 activity reprogram normal fibroblasts into CAFs, these findings deepen our understanding of the dynamic interactions within the TME. This finding has important implications for future cancer therapies.

Here, we focused on cluster 1 and 2 CAFs because of their abundance in the TME and identified NCAM1$^+$αSMA$^+$ CAFs as a representative of the combination of these two clusters. Although αSMA is a well-known marker for myofibroblasts, NCAM1 expression has been less characterized in CAFs. Our re-analysis of scRNA-seq data of breast CAF clusters from MMTV-PyMT breast tumor model by Foster et al. [38]. revealed that *Ncam1* was specifically expressed in MR CAFs (Supplementary Fig. 3A), which exhibit myofibroblast phenotypes[38] and share common genes with our mouse breast NCAM1$^+$αSMA$^+$ CAFs. Moreover, we observed that NCAM1 was expressed in the breast CAFs of human breast tumor tissues (Fig. 6A). These findings suggest NCAM1 as a beneficial conserved cell surface marker for the immunosuppressive CAF subpopulation in mouse and human breast tumors.

Using LATS1/2-deficient 4T1 breast cancer model, we showed that TGFβ-expressing NCAM1$^+$αSMA$^+$ CAFs are associated with the dysfunctionality of CD8$^+$ T cells and tumor progression. Previous studies have convincingly demonstrated the important functions of TGFβ in T cell suppression. For instance, TGFβ directly suppresses CD8$^+$ T cell function by activating SMAD and AFT1 transcription factors to repress the expression of effector cytokines such as granzyme B and IFNγ[40]. Additionally, TGFβ enhances the expression of the inhibitory receptor PD-1 in CD8$^+$ T cells[41]. Recent in vivo studies on multiple cancer types, including breast cancer, have shown that blocking TGFβ increases the T cell activity and enhances the response to immune checkpoint inhibitors, thereby significantly inhibiting the tumor growth[42–44]. Depletion of TGFβ-expressing CAFs (named LRRC15$^+$ CAFs) promotes CD8$^+$ T cell function and significantly suppresses the growth of pancreatic ductal adenocarcinoma[30]. Furthermore, gene signatures of the TGFβ-expressing CAF subset in human breast cancer correlate with poor response to immunotherapy in patients with melanoma[45]. Our findings, together with those of recent studies, suggest that targeting the TGFβ-expressing CAF subset may enhance the efficacy of immune checkpoint blockade therapy.

Limitations of the study include the methods employed for tumor dissociation and cell sorting, which utilized negative gating with predefined markers to isolate stromal cells. While these are standard techniques for scRNA-seq sample preparation, they may result in the exclusion of certain cell subpopulations, potentially limiting the comprehensive identification of stromal cells in our analysis. Additionally, our study focused specifically on a single time point (16 days post-transplantation) to investigate cancer progression. Given the dynamic nature of tumor development, the composition and functions of CAFs can change over time. Thus, our findings may not fully capture changes in CAF subpopulations at different stages of tumor growth, which could impact the interpretation of CAF heterogeneity influenced by the cancer cell-intrinsic Hippo pathway. Moreover, although our study demonstrated that LATS1/2 in cancer cells associate with NCAM1$^+$αSMA$^+$ CAFs and T cell dysfunction, it remains unclear whether the reduction in these CAFs alone is responsible for the observed T cell activation and consequent tumor suppression in LATS1/2 dKO tumors. Further mechanistic investigations, including determining the YAP/TAZ-dependency of observed changes in CAF composition, as well as the importance of TGFβ in T cell suppression, are essential to understand the precise molecular mechanisms linking the Hippo pathway to CAF heterogeneity and their interaction with immune responses. Given the considerable heterogeneity of cancer, investigating the Hippo pathway status along with NCAM1 and αSMA expression within tumor tissues could provide insights into the specific association between NCAM1$^+$αSMA$^+$ CAFs and the Hippo pathway in breast cancer tissues. Furthermore, the study's generalizability is constrained by the limited size of the patient cohort examined. As such, correlations between our experimental findings and clinical outcomes remain uncertain. Additionally, our primary conclusions were drawn from analyses using a mouse 4T1 breast cancer model, re-analysis of scRNA-seq data from the mouse MMTV-PyMT breast tumor model, and a small subset of human breast cancer patient samples. Future research should thus explore whether NCAM1$^+$αSMA$^+$ CAFs are present in other cancer types and investigate their potential roles in cancer progression. Notably, although NCAM1$^+$αSMA$^+$ CAFs were observed in only a small number of breast cancer samples in our cohort (three out of 27 samples), all of those cases were associated with metastasis and advanced stage IV disease (Supplementary Table 2), suggesting that NCAM1 + αSMA + CAFs may play a role in poor patient prognosis. Therefore, further studies are warranted to evaluate the therapeutic potential of targeting NCAM1$^+$αSMA$^+$ CAFs to enhance immunotherapy responses.

Methods

Animals

Female BALB/c and C57BL/6 mice (7–10 weeks old) were purchased from Kyudo Co., Ltd. (Saga, Japan). All animal experiments were approved by the Kumamoto University Institute of Resource Development and Analysis Center for Animal Resources and Development. Animals were housed in specific pathogen free area in Center for Animal Resources and Development (CARD), Kumamoto University. We have complied with all relevant ethical regulations for animal use.

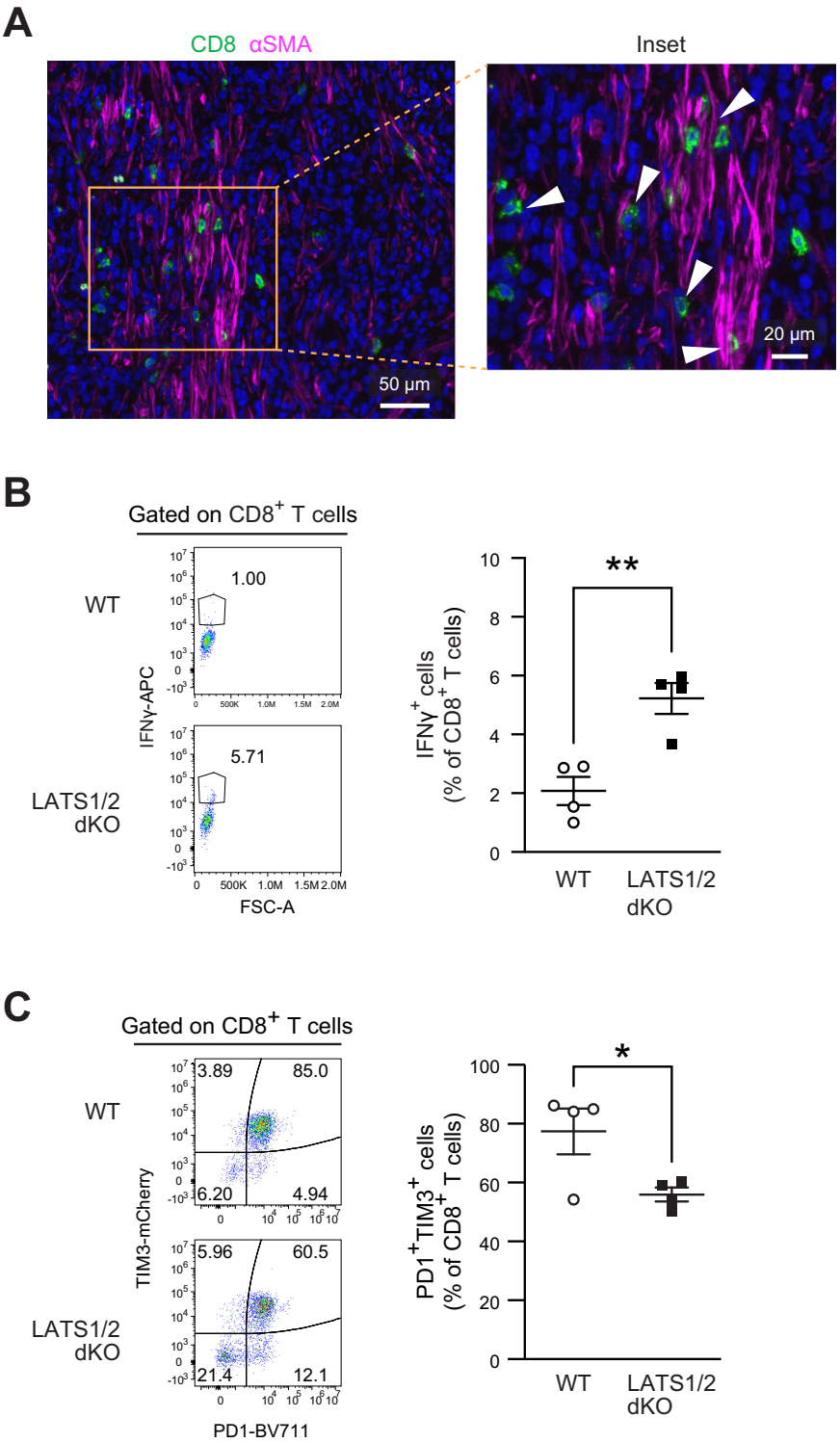

Fig. 5 | Dysfunctional CD8$^+$ T cells are abundant in NCAM1$^+$αSMA$^+$ CAFs-enriched tumors. **A** Representative immunofluorescence images of mouse breast tumor samples. Frozen sections of WT 4T1 breast tumors were subjected to immunostaining analysis of CD8 (green) and αSMA (magenta) or DAPI for DNA (blue). Data are representative of three tumors. Scale bar = 50 μm; inset scale bar = 20 μm. **B** WT or LATS1/2 dKO 4T1 breast cancer cells were injected into BALB/c mice, and tumors were then subjected to flow cytometry to analyze IFNγ expression at 16 days after transplantation. Representative scatterplots of the gated CD8$^+$ T cells are shown in the left panel. Data are represented as the mean ± SEM; $n = 4$ samples; pooled 4–12 tumors in each group. $^*p < 0.05$, unpaired two-tailed t-test. **C** Tumors were prepared as in **B** and subjected to flow cytometry to analyze PD1 and TIM3 expression. Representative scatterplots of the gated CD8$^+$ T cells are shown in the left panel. Data are represented as the mean ± SEM; $n = 4$ samples; pooled 4–6 tumors in each group. $^*p < 0.05$, unpaired two-tailed t-test.

Cell lines

4T1 cells were cultured in the Roswell Park Memorial Institute (RPMI)-1640 medium (#189-02025; Wako) supplemented with 10% fetal bovine serum (FBS; #173012; SIGMA), penicillin (100 U/mL), and streptomycin (100 mg/mL). NIH3T3 cells were cultured in Dulbecco's modified Eagle's medium (DMEM; #044-29765; Wako) supplemented with 10% FBS (#173012; SIGMA), penicillin (100 U/mL), and streptomycin (100 mg/mL). All cell lines were cultured under an atmosphere of 5% CO_2 at 37 °C.

Collection of human tumor tissues

A total of 27 paraffin-embedded breast tumor tissue samples and clinicopathological data (Supplementary Table 2) were collected with ethical approval from the Siriraj Institutional Review Board (COA no. Si 580/2018 and Si 542/2022). All clinical data were collected after ethical approval. Tissue samples were collected from patients who provided informed consent prior to surgery. All ethical regulations relevant to human research participants were followed.

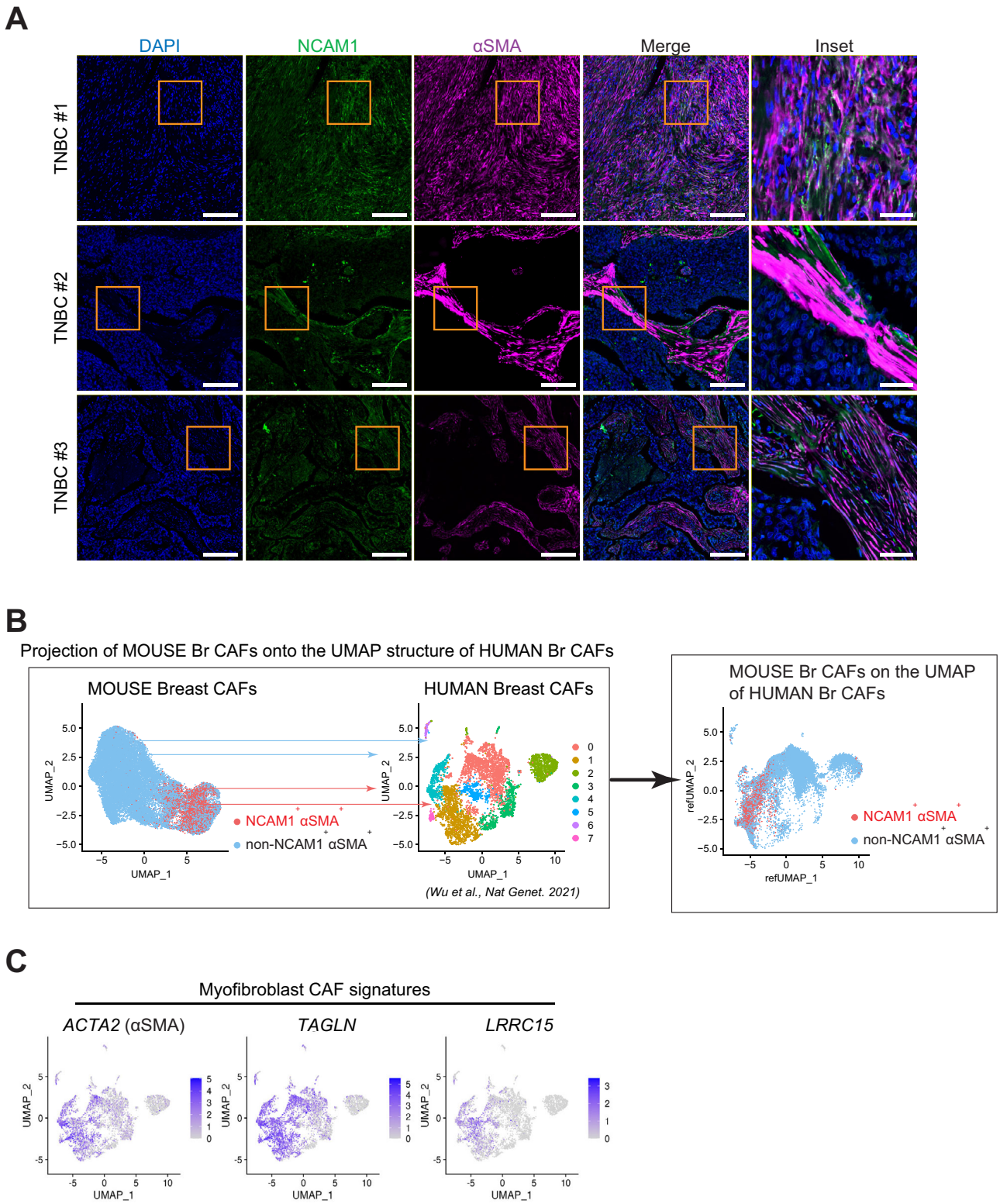

Fig. 6 | NCAM1$^+$αSMA$^+$ CAFs are observed in human breast cancer. **A** Representative immunofluorescence images of three positive cases with NCAM1 and αSMA co-expression ($n = 27$ patients with breast cancer). Formalin-fixed paraffin-embedded tissue sections of breast tumors were subjected to immunostaining of NCAM1 (green) and αSMA (magenta) or DAPI for DNA (blue). Scale bar = 200 μm; inset scale bar = 50 μm. **B** Cell type label transfer and projection of mouse breast CAF clusters onto the UMAP structure of human breast CAF clusters[38]. Colors correspond to the indicated CAF cluster. **C** Feature plot showing the single cells with indicated gene expression on the UMAP plot of human breast CAF clusters. Color indicates the expression level (blue indicates high expression).

Gene deletion using the CRISPR/Cas9 system

LATS1/2-deleted 4T1 cells were generated as previously described[13]. Deletion of LATS1/2 in 4T1 breast cancer cells was confirmed by DNA mutation, lack of protein expression, and decreased activity of LATS1/2 as determined via Sanger sequencing, immunoblot analysis, and immunofluorescence staining, respectively.

Orthotopic transplantation of tumor cells

Briefly, 4T1 cells (5×10^5) were transplanted into the mammary fat pads of 7–10 week-old BALB/c mice. The tumor size was monitored and measured using calipers every 2–3 days. Mice were sacrificed at day 16 post-transplantation where tumors did not exceed maximum permitted size (15 mm in diameter).

Tumor dissociation and cell isolation

On day 16 after orthotopic transplantation, WT or LATS1/2 dKO 4T1 tumors were harvested and pooled from nine tumor-bearing mice for each condition. The tumor samples were minced and dissociated using an enzymatic solution containing 30 µg/mL DNase I (#LS002139; Worthington), 1 mg/mL collagenase type I (#LS004196; Worthington), and 0.6 U/mL Dispase II (#17105041; Gibco) in RPMI. The samples were incubated at 37 °C for 25 min using a gentle MACS Octo Dissociator with Heaters (#130-096-427; Miltenyi Biotec). Tumor cells were washed with a fluorescence-activated cell sorting (FACS) buffer (2% heat-inactivated FBS in phosphate-buffered saline (PBS; calcium and magnesium-free), incubated with ACK (Ammonium-Chloride-Potassium) buffer for red blood cell lysis, and filtered through 100- and 70-µm cell strainers (#833945100 and #833945070; SARSTEDT) to obtain single-cell suspensions.

Stromal cell preparation for scRNA-seq

On day 16 after 4T1 transplantation, WT or LATS1/2 dKO 4T1 tumors were harvested and pooled from nine tumor-bearing mice for each condition (18 tumors each). Tumor cell suspensions were subjected to different processes to enrich the stromal cells for scRNA-seq. First, immune cells ($CD45^+$) were removed from the tumor cell samples using the positive selection-based magnetic bead method with MojoSort mouse CD45 nanobeads (#480028; BioLegend), according to the manufacturer's protocol. Briefly, the tumor cell suspensions were washed and resuspended in MojoSort buffer (#480017; BioLegend). The cells were then incubated with CD45 nanobeads for 15 min on ice, followed by the separation of labeled cells using a magnet. The remaining cell suspensions were incubated in a mouse Fc block (anti CD16/CD32, clone 2.4G2) for 15 min on ice, followed by staining with fluorophore conjugated antibodies specific for the markers of immune cells (CD45, clone 30F-11), epithelial cancer cells (EpCAM, clone G8.8), and endothelial cells (CD31, clone 390) for 30 min on ice. The used antibodies are shown in Supplementary Table 3. Cells were stained with propidium iodide (PI; Dojindo) shortly before FACS. Cells were sorted using a BD FACSAria III cell sorter with 100-µm nozzle to avoid harsh cell flow condition. Stromal cells were enriched by excluding the dead cells with propidium iodide- and lineage-negative selection of CD45-EpCAM-CD31 cells. Stromal cells were sorted directly into PBS containing 2% bovine serum albumin (BSA) (#AM2616; Thermo Fisher Scientific).

scRNA-seq of mouse stromal cells

scRNA-seq library preparation was performed using the 10X Genomics Chromium system following the manufacturer's instructions (Chromium Next GEM Single Cell 3′ Reagent Kits v3.1 (Dual Index), 10X Genomics, PN-1000269). Two libraries for each WT and LATS1/2 dKO stromal sample were generated to enable the detection of CAF subsets with a very small number of cells. The sorted single-cell suspensions were washed and resuspended in PBS containing 0.04% BSA. A total of 14,000 cells (80% viability) per library were loaded into the 10X Chromium chips and processed on the Chromium Controller to form a gel bead-in-emulsion with approximately 8500 cells recovered. Reverse transcription and single-cell barcoding were performed for each bead-in-emulsion gel using a BioRad C1000 Touch thermocycler. The cDNA from the reverse transcription reaction was purified and amplified for 11 cycles. The cDNA products were then processed for size selection using the SPRIselect Reagent (#B23317; Beckman Coulter) and analyzed for quality and yield using the High Sensitivity D5000 TapeStation system (#5067-5592 and #5067-5593; Agilent). Libraries were constructed through end repair, A-tailing, adaptor ligation, sample index PCR, and double-sided size selection following the 10X Genomics user guide. The final library products were quantified using the NEBNext Library Quant Kit for Illumina (#E7630S; New England Biolabs), according to the manufacturer's protocol. Libraries were sequenced on a NovaSeq 6000 (Illumina) using paired-end sequencing and dual indexing.

scRNA-seq data processing and analysis

Raw Illumina BCL files were converted into FASTQ files using the Cell Ranger pipelines (10X Genomics). Reads were aligned with the mouse reference genome (mm10), and cell-associated barcodes and UMI were counted to generate matrix data using the Cell Ranger package. After processing the raw data, matrix data with approximately 20,000 mean reads per cell were obtained.

Downstream data analyses, including quality control, data integration, clustering, and data visualization, were performed using R (v.4.3.0) and Seurat (v.4.3.0, Satija lab)[39]. Cells with <200 features and >5% mitochondrial genes were removed, followed by data normalization using the Seurat *SCTransform* function for each dataset. All datasets were integrated using the Seurat SCTransform-based reciprocal PCA workflow with the top 3000 most variable features. PCA and UMAP were applied to the integrated data, which were subsequently clustered using the first 30 principal components of the dimensionality of the dataset. Based on this preliminary clustering, the expression of cell-type-specific markers was broadly divided into four groups: immune cells (*Ptprc*), pericytes (*Rgs5*), cancer cells with loss of EpCAM expression (*Krt7* and *Krt8*), and fibroblasts (*Pdpn* and *Pdgfra*). The $Pdpn^+$ population was then re-clustered to further characterize the CAFs. PCA with highly variable features defined in the CAF groups and UMAP were run on the data, and CAF clusters were generated using the first 30 principal components and a resolution of 0.3. Differentially expressed markers for each cluster were identified with the *FindMarkers* function using the default Wilcoxon rank-sum test for identifying differentially expressed genes and the Bonferroni correction method for p-value adjustment. A heatmap of the top ten markers for each CAF cluster was visualized using the *DoHeatmap* function. The co-expression of the two genes was visualized using the *FeaturePlot* function with the *blend* parameter.

Pathway enrichment analysis

Differentially expressed genes for each cluster with an average log2(fold-change) > 0.25 identified by the *FindMarkers* function, were used to perform GO analysis using the clusterProfiler package (v.4.8.2)[46]. The *compareCluster* function was used to compare the enriched GO among the clusters. GO terms with adjusted *P*-value below 0.05 were considered significantly enriched by DEGs.

Gene set enrichment analysis

For the comparison between $NCAM1^+\alpha SMA^+$ CAFs and either myCAFs, iCAFs, or apCAFs from Elyada et al. [29], the fibroblast-enriched expression data was downloaded from GSE129455 and used for clustering using the first 20 principal components and a resolution of 0.2. Differentially expressed markers for each cluster with an average log2(fold-change) > 0.25 were identified using the *FindMarkers* function. For the comparison with $LRRC15^+$ CAFs, the marker list from Krishnamurty et al. [30] was used. Marker gene lists from each published cluster were customized for enrichment analysis based on a gene matrix-transposed file format. Gene set enrichment of each published cluster signature within $NCAM1^+\alpha SMA^+$ CAFs or non-$NCAM1^+\alpha SMA^+$ CAFs was evaluated using the fgsea package with the default parameters[47].

Seurat multimodal reference mapping analysis

To acquire human breast CAF clusters, the published scRNA-seq data of 26 primary tumors from patients with breast cancer by Wu and colleagues[38] were downloaded from GSE176078. The human scRNA-seq dataset included all tumor cell types. The expression matrix data of the stromal cells were extracted using the barcode names of the stromal clusters downloaded from https://singlecell.broadinstitute.org/single_cell/study/SCP1039 provide by Wu and colleagues. Human gene names in the expression matrix data were converted to mouse gene names using the homologene database. This expression matrix data were then used to create Seurat objects of human stromal cells. The data were normalized using the Seurat *SCTransform* function. PCA and UMAP were performed on the data, and low-resolution stromal clusters were generated using the first 30 principal components. Reclustering was performed to generate the human CAF clusters. First, CAFs were identified based on cell type-specific markers according to a previously published study: CAFs (*PDGFRA* and *COL1A1*), perivascular-like cells (*MCAM* and *PDGFRB*), and endothelial cells (*PECAM1*). PCA with new variable features and UMAP were applied to the data, and human CAF clusters were generated using the first 30 principal components at a resolution of 0.2. Seurat reference mapping was then implemented to integrate and transfer the cell-type labels of mouse breast CAF clusters onto the UMAP structure of human breast CAF clusters using default parameters[39].

Flow cytometry

Cell suspensions were stained with the LIVE/DEAD Fixable Near-IR Dead Cell Stain Kit (#L34976; Thermo Fisher Scientific) for 15 min on ice, followed by blocking with a mouse Fc block (anti CD16/CD32, clone 2.4G2) prior to staining. Fluorophore conjugated antibody CD45 (clone 30F-11), CD3 (clone 17A2 or clone 145-2C11), CD8a (clone 53-6.7), CD279 (PD-1) (clone J43), CD366 (Tim-3) (clone B8.2C12), Granzyme B (clone GB11), and IFNγ (clone XMG1.2), EpCAM (clone G8.8), CD31 (clone 390), podoplanin (PDPN, clone 8.1.1), platelet-derived growth factor receptor-α (PDGFR-α, clone APA5), and alpha smooth muscle actin (αSMA, clone 1A4) antibodies were used following the manufacturers protocol. The cells were stained with primary antibody against anti-NCAM1 (CD56, clone E7X9M), and a BV421 goat anti-rabbit IgG secondary antibody (#565014; BD Biosciences) was used according to the manufacturer's protocol. The used antibodies are listed in Supplementary Table 3. For intracellular staining, cells were fixed and permeabilized using a Foxp3/transcription factor staining buffer kit (#00-5523-00; Thermo Fisher Scientific). To evaluate intracellular cytokine expression, cell suspensions were incubated with the protein transport inhibitor (#555029; BD biosciences) for 4 h prior to cytokine staining.

Flow cytometry was performed using CytoFLEX S (Beckman Coulter) and the results were analyzed using FlowJo software (BD Biosciences). The gating strategy for the flow cytometry analysis was shown in Supplementary Fig. 9.

Immunofluorescence analysis of 4T1 cells

Cells were treated with 1 μg/mL LatB for 1 h. Cells were fixed with 4% paraformaldehyde in PBS for 10 min at room temperature and permeabilized with 0.1% Triton X-100 in PBS for 10 min at room temperature. Cells were then incubated with primary antibodies to YAP/TAZ (#sc-101199; Santa Cruz Biotechnology) for overnight at 4 °C and subsequently incubated with Alexa Fluor 488-labeled goat secondary antibodies for 90 min at room temperature. Cells were mounted in Fluoromount (#K024; Cosmobio) with DAPI (Invitrogen) for observation.

Immunofluorescence analysis of mouse tumors

To prepare paraffin-embedded tissues, tumors were fixed with 10% formalin neutral buffer solution (#062-01661; Wako), embedded in paraffin, and sectioned using a microtome, according to standard procedures. For preparation of frozen tissues, tumors were embedded in optimal cutting temperature medium (#45833; Sakura Finetek), frozen for storage at −80 °C and cryosectioned. Before immunostaining, paraffin-embedded tissue sections were deparaffinized and rehydrated, and antigen retrieval was performed using Tris-EDTA buffer (pH 9.0). The frozen cryostat sections were air-dried for 1 h and fixed with methanol for 10 min. For immunostaining, sections were blocked with PBS with 1% BSA and then stained with the following antibodies overnight at 4 °C: fluorophore conjugated antibody alpha smooth muscle actin (αSMA, clone 1A4), CD8a (clone 53-6.7), anti-NCAM1 (CD56, clone E7X9M), anti-TGF beta 1 (clone EPR21143). After washing with PBS, the sections were stained with the secondary antibody, goat anti-rabbit Alexa Fluor 546 (Thermo Fisher Scientific, A11035), for 2 h at room temperature. Sections were washed with PBS and mounted in Fluoromount (#K024; Cosmobio) with DAPI (Invitrogen) for observation. Images were acquired and quantified using a KEYENCE BZ-X800 system. The antibodies used in this study are shown in Supplementary Table 3.

Immunohistochemical analysis of mouse tumors

Paraffin-embedded sections of 4T1 breast tumors were deparaffinized and rehydrated, followed by antigen retrieval using citrate buffer (pH 6.0). Sections were blocked with PBS with 1% BSA and then stained with YAP/TAZ antibody (#93622; Cell Signaling Technology) overnight at 4°C. Sections were developed using Peroxidase Stain DAB solution (#25985-50; nacalai), with counterstain using hematoxylin. Images were acquired using a KEYENCE BZ-X800.

Immunofluorescence analysis of human tissues

Formalin-fixed, paraffin-embedded tissue sections from 27 human breast tumors were deparaffinized and rehydrated, and antigen retrieval was performed using EnVision FLEX target retrieval solution (#K8005; Agilent Dako). For immunostaining, sections were blocked with Intercept (PBS) blocking buffer (#927-70001; Licor) and stained with the fluorophore-conjugated antibody alpha smooth muscle actin (αSMA, clone 1A4) and anti-NCAM1 (CD56, clone E7X9M) overnight at 4 °C, followed by staining with secondary donkey anti-rabbit Alexa 488 antibody (A21206; Invitrogen) and DAPI (Invitrogen) for nuclear Images were obtained with a CyteFinder II HT (Rarecyte) and analyzed using Qupath[48]. The antibodies used in this study are shown in Supplementary Table 3.

Generation of TGF-β-overexpressing fibroblasts

Human full-length TGFβ1 was cloned into the pBluescript plasmid. To substitute cysteines at amino acid positions 223 and 225 to serines to achieve constitutive expression of biologically active TGFβ1[36], site-directed mutagenesis PCR was performed using PrimeSTAR HS DNA Polymerase (#R010A; Takara). The TGFβ1 mutant segment was subcloned into the lentiviral vector plasmid pLVSIN-CMV-Pur. NIH3T3 cells stably expressing empty vector or TGFβ1 mutant vector were generated by lentiviral infection. Lentiviral transfer plasmids were co-transfected with packaging plasmids pLenti-P2A and pLenti-P2B (#LV003; Cosmobio) into HEK293T cells using a PolyJet (#SL100688; SignaGen). Forty-eight hours after transfection, the lentiviral supernatant was supplemented with 5 μg/mL polybrene, passed through a 0.45 mm filter, and used for infection. Forty-eight hours after infection, NIH3T3 cells with the target gene construct were selected with 5 μg/mL puromycin (#A1113803; Thermo Fisher Scientific) in culture medium. To confirm successful TGFβ1 overexpression, the protein level expression of TGFβ1 in the cells or culture medium was evaluated using immunoblot analysis.

Immunoblot analysis

Cells or culture medium were dissolved in a lysis buffer (0.5% Triton X-100, 50 mM Tris-HCl pH 7.5, and 150 mM NaCl) with protease inhibitors (10 μM leupeptin, 1 μM pepstatin A, and 1 mM phenylmethylsulfonyl fluoride). Equal amounts of proteins were resolved via sodium dodecyl sulfate-polyacrylamide gel electrophoresis under reducing conditions, unless otherwise mentioned in the Figure Legends. Antibodies against LATS1 (#3477; Cell Signaling Technology), YAP (#14074; Cell Signaling Technology), actin (#ab3280; Abcam), TGFβ1 (#215715; Abcam), and

HSP90 (#610418; BD Biosciences) were used. The used antibodies are listed in Supplementary Table 3. Phos-tag electrophoresis was performed, as previously described[49]. YAP can be separated into multiple bands based on its differential phosphorylation levels. Where indicated, cells were treated with 1 μg/mL LatB or 25 mM 2-deoxy-D-glucose (2-DG) for 1 h before harvest. Images were acquired using the ChemiDoc Touch imaging system (Bio-Rad Laboratories). The whole western blotting images were provided in Supplementary Figs. 10 and 11.

Fibroblast-immune cell co-culture

TGF-β1-overexpressing NIH3T3 or control NIH3T3 cells (2×10^4) were seeded in a 96-well plate in DMEM supplemented with 10% FBS. Twenty-four hours after seeding, the medium was changed to a 1:1 ratio of DMEM supplemented with 10% FBS and RPMI-1640 medium supplemented with 10% FBS. After culturing in the mixed medium for 24 h, splenocytes (2.75×10^5) were co-cultured with fibroblast cells in the presence of CD3/CD28 Dynabeads (#11452D; Gibco) in RPMI-1640 medium supplemented with 10% FBS. After incubation for 3 days, the magnetic beads were removed, and splenocytes were stimulated with 25 ng/mL PMA and 1 μg/mL ionomycin for 1 h. Subsequently, intracellular cytokine (IFNγ and granzyme B) expression was evaluated by flow cytometry analysis, as described above.

Statistics and reproducibility

Statistical analyses were conducted using the GraphPad Prism 9 software (GraphPad Software, USA). All statistical parameters and methods are reported in the Figures and the Figure Legends. A value of $p < 0.05$ was considered to be statistically significant. Sample sizes and number of replicates are reported in the Figure Legends.

Reporting summary

Further information on research design is available in the Nature Portfolio Reporting Summary linked to this article.

Data availability

The scRNA-seq data generated in this study have been deposited in the DNA Data Bank of Japan (DDBJ) at DRA017669 and E-GEAD-666. The source data related to Figs. 1A, 2E, 4C, 4F, 5B, and 5C are presented in Supplementary Data 3. The uncropped blots related to Fig. 4E and Supplementary Fig. 1B are provided in Supplementary Figs. 10 and 11 respectively. All other raw data generated in this study are available from the corresponding author upon request.

Received: 30 January 2024; Accepted: 10 October 2024;
Published online: 17 October 2024

References

1. Hanahan, D. & Weinberg, R. A. Hallmarks of Cancer: The Next Generation. *Cell* **144**, 646–674 (2011).
2. Vinay, D. S. et al. Immune evasion in cancer: Mechanistic basis and therapeutic strategies. *Semin. Cancer Biol.* **35**, S185–S198 (2015).
3. Caligiuri, G. & Tuveson, D. A. Activated fibroblasts in cancer: Perspectives and challenges. *Cancer Cell* **41**, 434–449 (2023).
4. Sahai, E. et al. A framework for advancing our understanding of cancer-associated fibroblasts. *Nat. Rev. Cancer* **20**, 174–186 (2020).
5. Chhabra, Y. & Weeraratna, A. T. Fibroblasts in cancer: Unity in heterogeneity. *Cell* **186**, 1580–1609 (2023).
6. Chen, Y., McAndrews, K. M. & Kalluri, R. Clinical and therapeutic relevance of cancer-associated fibroblasts. *Nat. Rev. Clin. Oncol.* **18**, 792–804 (2021).
7. Harvey, K. F., Zhang, X. & Thomas, D. M. The Hippo pathway and human cancer. *Nat. Rev. Cancer* **13**, 246–257 (2013).
8. Moroishi, T., Hansen, C. G. & Guan, K.-L. The emerging roles of YAP and TAZ in cancer. *Nat. Rev. Cancer* **15**, 73–79 (2015).
9. Meng, Z., Moroishi, T. & Guan, K. L. Mechanisms of Hippo pathway regulation. *Genes Dev* **30**, 1–17 (2016).
10. Johnson, R. & Halder, G. The two faces of Hippo: targeting the Hippo pathway for regenerative medicine and cancer treatment. *Nat. Rev. Drug Discov.* **13**, 63–79 (2014).
11. Ma, S. et al. Hippo signalling maintains ER expression and ER+ breast cancer growth. *Nature* **591**, E1–E10 (2021).
12. Li, F.-L. & Guan, K.-L. The two sides of Hippo pathway in cancer. *Semin. Cancer Biol.* **85**, 33–42 (2022).
13. Moroishi, T. et al. The Hippo pathway kinases LATS1/2 suppress cancer immunity. *Cell* **167**, 1525–1539.e1517 (2016).
14. Sugimoto, H., Mundel, T. M., Kieran, M. W. & Kalluri, R. Identification of fibroblast heterogeneity in the tumor microenvironment. *Cancer Biol Ther* **5**, 1640–1646 (2006).
15. Meng, Z. et al. MAP4K family kinases act in parallel to MST1/2 to activate LATS1/2 in the Hippo pathway. *Nat. Commun.* **6**, 8357 (2015).
16. Buechler, M. B. et al. Cross-tissue organization of the fibroblast lineage. *Nature* **593**, 575–579 (2021).
17. Dey, A., Varelas, X. & Guan, K.-L. Targeting the Hippo pathway in cancer, fibrosis, wound healing and regenerative medicine. *Nat. Rev. Drug Discov.* **19**, 480–494 (2020).
18. Augsten, M. et al. CXCL14 is an autocrine growth factor for fibroblasts and acts as a multi-modal stimulator of prostate tumor growth. *Proc. Natl. Acad. Sci. USA.* **106**, 3414–3419 (2009).
19. Dou, C. et al. P300 acetyltransferase mediates stiffness-induced activation of hepatic stellate cells into tumor-promoting myofibroblasts. *Gastroenterology* **154**, 2209–2221.e2214 (2018).
20. Zhang, J. et al. ATF3-activated accelerating effect of LINC00941/lncIAPF on fibroblast-to-myofibroblast differentiation by blocking autophagy depending on ELAVL1/HuR in pulmonary fibrosis. *Autophagy* **18**, 2636–2655 (2022).
21. Chang, A. L. et al. CCL2 produced by the glioma microenvironment is essential for the recruitment of regulatory T cells and myeloid-derived suppressor cells. *Cancer Res* **76**, 5671–5682 (2016).
22. Gschwandtner, M., Derler, R. & Midwood, K. S. More than just attractive: how CCL2 influences myeloid cell behavior beyond chemotaxis. *Front. Immunol* **10**, 2759 (2019).
23. Oo, M. W. et al. Resident stroma-secreted chemokine CCL2 governs myeloid-derived suppressor cells in the tumor microenvironment. *JCI Insight* **7**, e148960 (2022).
24. Houthuijzen, J. M. et al. CD26-negative and CD26-positive tissue-resident fibroblasts contribute to functionally distinct CAF subpopulations in breast cancer. *Nat. Commun.* **14**, 1–21 (2023).
25. Grinnell, F. Fibroblasts, myofibroblasts, and wound contraction. *J. Cell Biol* **124**, 401–404 (1994).
26. Rockey, D. C., Weymouth, N. & Shi, Z. Smooth muscle α actin (Acta2) and myofibroblast function during hepatic wound healing. *PLOS ONE* **8**, e77166 (2013).
27. Miyazaki, Y. et al. Adipose-derived mesenchymal stem cells differentiate into heterogeneous cancer-associated fibroblasts in a stroma-rich xenograft model. *Sci. Rep* **11**, 4690 (2021).
28. Foster, D. S. et al. Multiomic analysis reveals conservation of cancer-associated fibroblast phenotypes across species and tissue of origin. *Cancer Cell* **40**, 1392–1406.e1397 (2022).
29. Elyada, E. et al. Cross-species single-cell analysis of pancreatic ductal adenocarcinoma reveals antigen-presenting cancer-associated fibroblasts. *Cancer Discov* **9**, 1102–1123 (2019).
30. Krishnamurty, A. T. et al. LRRC15+ myofibroblasts dictate the stromal setpoint to suppress tumour immunity. *Nature* **611**, 148–154 (2022).
31. Öhlund, D. et al. Distinct populations of inflammatory fibroblasts and myofibroblasts in pancreatic cancer. *J. Exp. Med.* **214**, 579–596 (2017).
32. Huang, H. et al. Mesothelial cell-derived antigen-presenting cancer-associated fibroblasts induce expansion of regulatory T cells in pancreatic cancer. *Cancer Cell* **40**, 656–673.e657 (2022).
33. Batlle, E. & Massagué, J. Transforming growth factor-β signaling in immunity and cancer. *Immunity* **50**, 924–940 (2019).

34. Crawford, S. E. et al. Thrombospondin-1 Is a Major Activator of TGF-β1 In Vivo. *Cell* **93**, 1159–1170 (1998).
35. Travis, M. A. & Sheppard, D. TGF-β activation and function in immunity. *Annu. Rev. Immunol.* **32**, 51–82 (2014).
36. Brunner, A. M., Marquardt, H., Malacko, A. R., Lioubin, M. N. & Purchio, A. F. Site-directed Mutagenesis of Cysteine Residues in the Pro Region of the Transforming Growth Factor β1 Precursor: Expression and Characterization of Mutant Proteins. *J. Biol. Chem.* **264**, 13660–13664 (1989).
37. Wolf, Y., Anderson, A. C. & Kuchroo, V. K. TIM3 comes of age as an inhibitory receptor. *Nat. Rev. Immunol.* **20**, 173–185 (2020).
38. Wu, S. Z. et al. A single-cell and spatially resolved atlas of human breast cancers. *Nat. Genet.* **53**, 1334–1347 (2021).
39. Hao, Y. et al. Integrated analysis of multimodal single-cell data. *Cell* **184**, 3573–3587.e3529 (2021).
40. Thomas, D. A. & Massague, J. TGF-beta directly targets cytotoxic T cell functions during tumor evasion of immune surveillance. *Cancer Cell* **8**, 369–380 (2005).
41. Park, B. V. et al. TGFbeta1-Mediated SMAD3 Enhances PD-1 Expression on Antigen-Specific T Cells in Cancer. *Cancer Discov* **6**, 1366–1381 (2016).
42. Tauriello, D. V. F. et al. TGFβ drives immune evasion in genetically reconstituted colon cancer metastasis. *Nature* **554**, 538–543 (2018).
43. Mariathasan, S. et al. TGFβ attenuates tumour response to PD-L1 blockade by contributing to exclusion of T cells. *Nature* **554**, 544–548 (2018).
44. Grauel, A. L. et al. TGFβ-blockade uncovers stromal plasticity in tumors by revealing the existence of a subset of interferon-licensed fibroblasts. *Nat. Commun.* **11**, 6315 (2020).
45. Kieffer, Y. et al. Single-cell analysis reveals fibroblast clusters linked to immunotherapy resistance in cancer. *Cancer Discov* **10**, 1330–1351 (2020).
46. Yu, G., Wang, L. G., Han, Y. & He, Q. Y. clusterProfiler: an R Package for Comparing Biological Themes Among Gene Clusters. *OMICS* **16**, 284–287 (2012).
47. Gennady, K. et al. Fast gene set enrichment analysis. *Posted on bioRxiv*, https://doi.org/10.1101/060012 (2021).
48. Bankhead, P. et al. QuPath: Open source software for digital pathology image analysis. *Sci. Rep* **7**, 16878 (2017).
49. Moroishi, T. et al. A YAP/TAZ-induced feedback mechanism regulates Hippo pathway homeostasis. *Genes Dev* **29**, 1271–1284 (2015).

Acknowledgements

We thank Research Promotion Unit, Medical Institute of Bioregulation, Kyushu University for assistance with Illumina sequencing.; Pranisa Jamjuntra for technical support in the immunofluorescence analysis of human tissues; Taishi Yamane, Hao Li, Yudai Ohta, Mohamed Fathi Saleh, Saisai Liu, Takashi Matsumoto, and Shuran Li for discussion; Emi Kosano for creating the mouse image in Fig. 1B. This work was supported by grants from the Japan Agency for Medical Research and Development (AMED) PRIME (JP22gm6210030 to T.M.), Japan Science and Technology Agency (JST) FOREST (JPMJFR226J to T.M.), Japan Society for the Promotion of Science (JSPS) KAKENHI (22H05635, 24H00864, and 24H00865 to T.M.), Takeda Science Foundation (to T.M.), and Kobayashi Foundation for Cancer Research (to T.M.). Additionally, this study received the Cross Frontier Research Grant from Kumamoto University (to T.M.), Center for Metabolic Regulation of Healthy Aging (CMHA) Research Grants (to T.M. and C.Thinyakul), and MidCareer Research Grant from the National Research Council of Thailand and Mahidol University (N42A650343 to C.Thuwajit.). C. Thinyakul is a recipient of the MEXT scholarship from the Japanese government and Mahidol University-Kumamoto University Dual Ph.D. program scholarship from Mahidol University and Kumamoto University.

Author contributions

Conceptualization: C.Thinyakul. and T.M.; methodology: C.Thinyakul. and T.M.; scRNA-seq analysis: C.Thinyakul., O.R., Y.L., A.N., A.M, Y.Sato., and K.I.N.; formal analysis: C.Thinyakul., Y.Sakamoto., M.S. Y.Kanamori., A.N., and T.M.; investigation: C.Thinyakul, M.N., S.T., R.S., S.S., P.C., and D.N.; writing—original draft: C.Thinyakul., Y.Sakamoto., and T.M.; Writing—reviewing and editing: C.Thinyakul., Y.Sakamoto., M.S., Y.L., S.T., O.R., A.N., R.S., S.S., A.M., P.C., D.N., M.N., Y.Kanamori., P.T., K.I.N., K.-L.G., Y.Sato., C.Thuwajit., and T.M.; funding acquisition: C.Thinyakul., C.Thuwajit. and T.M.; Supervision: C.Thuwajit. and T.M.

Competing interests

The authors declare the following competing interests: K.-L.G. is a co-founder of and holds an equity interest in Vivace Therapeutics. T.M. is an Editorial Board Member for Communications Biology, but was not involved in the editorial review of, nor the decision to publish this article. All other authors declare no competing interests.

Additional information

Supplementary information The online version contains supplementary material available at https://doi.org/10.1038/s42003-024-07041-4.

Correspondence and requests for materials should be addressed to Toshiro Moroishi.

Peer review information *Communications Biology* thanks Lu Han and the other, anonymous, reviewers for their contribution to the peer review of this work. Primary Handling Editor: Manuel Breuer.

[1]Department of Molecular and Medical Pharmacology, Faculty of Life Sciences, Kumamoto University, Kumamoto 860-8556, Japan. [2]Department of Immunology, Faculty of Medicine Siriraj Hospital, Mahidol University, Bangkok 10700, Thailand. [3]Siriraj Center of Research Excellence for Cancer Immunotherapy, Research Department, Faculty of Medicine Siriraj Hospital, Mahidol University, Bangkok 10700, Thailand. [4]Division of Genomics and Transcriptomics, Joint Research Center for Human Retrovirus Infection, Kumamoto University, Kumamoto 860-0811, Japan. [5]Division of Cellular Dynamics, Medical Research Laboratory, Institute of Science Tokyo, Bunkyo-ku, Tokyo 113-8510, Japan. [6]SirirajCenter of Research Excellence for Systems Pharmacology, Department of Pharmacology, Faculty of Medicine Siriraj Hospital, Mahidol University, Bangkok 10700, Thailand. [7]Department of Molecular and Cellular Biology, Medical Institute of Bioregulation, Kyushu University, Higashi-ku, Fukuoka 812-8582, Japan. [8]Anticancer Strategies Laboratory, Advanced Research Initiative, Institute of Science Tokyo, Bunkyo-ku, Tokyo 113-8510, Japan. [9]School of Life Sciences, Westlake University, Hangzhou 310030, China. [10]Center for Metabolic Regulation of Healthy Aging, Faculty of Life Sciences, Kumamoto University, Kumamoto, Kumamoto 860-8556, Japan. [11]These authors contributed equally: Yasuhisa Sakamoto, Mayuko Shimoda. moroishi@kumamoto-u.ac.jp